Oscillatory phase coupling coordinates anatomically dispersed functional cell assemblies

Ryan T. Canolty[a,b], Karunesh Ganguly[a,b,c,d], Steven W. Kennerley[b], Charles F. Cadieu[b,e], Kilian Koepsell[b,e], Jonathan D. Wallis[b,f], and Jose M. Carmena[a,b,g,1]

[a]Electrical Engineering and Computer Sciences, University of California, Berkeley, CA 94720; [b]Helen Wills Neuroscience Institute, University of California, Berkeley, CA 94720; [c]San Francisco Veterans Affairs Medical Center, San Francisco, CA 94121; [d]Department of Neurology, University of California, San Francisco, CA 94143; [e]Redwood Center for Theoretical Neuroscience, University of California, Berkeley, CA 94720; [f]Department of Psychology, University of California, Berkeley, CA 94720; and [g]Program in Cognitive Science, University of California, Berkeley, CA 94720

Hebb proposed that neuronal cell assemblies are critical for effective perception, cognition, and action. However, evidence for brain mechanisms that coordinate multiple coactive assemblies remains lacking. Neuronal oscillations have been suggested as one possible mechanism for cell assembly coordination. Prior studies have shown that spike timing depends upon local field potential (LFP) phase proximal to the cell body, but few studies have examined the dependence of spiking on distal LFP phases in other brain areas far from the neuron or the influence of LFP–LFP phase coupling between distal areas on spiking. We investigated these interactions by recording LFPs and single-unit activity using multiple microelectrode arrays in several brain areas and then used a unique probabilistic multivariate phase distribution to model the dependence of spike timing on the full pattern of proximal LFP phases, distal LFP phases, and LFP–LFP phase coupling between electrodes. Here we show that spiking activity in single neurons and neuronal ensembles depends on dynamic patterns of oscillatory phase coupling between multiple brain areas, in addition to the effects of proximal LFP phase. Neurons that prefer similar patterns of phase coupling exhibit similar changes in spike rates, whereas neurons with different preferences show divergent responses, providing a basic mechanism to bind different neurons together into coordinated cell assemblies. Surprisingly, phase-coupling–based rate correlations are independent of interneuron distance. Phase-coupling preferences correlate with behavior and neural function and remain stable over multiple days. These findings suggest that neuronal oscillations enable selective and dynamic control of distributed functional cell assemblies.

neuronal oscillations | neuronal ensembles | spike timing | local field potentials | brain rhythms

Significant progress has been made in understanding the dynamics and response properties of single nerve cells (1, 2) and how they interconnect to form cortical microcircuits (3, 4). More than 60 y ago, however, Donald Hebb hypothesized that the fundamental unit of brain operation is not the single neuron but rather the cell assembly—an anatomically dispersed but functionally integrated ensemble of neurons (5). The individual neurons that compose an assembly may reside in widely separated brain areas but act as a single functional unit through coordinated network activity. Dynamic interactions between multiple assemblies may then give rise to the large-scale functional networks found in mammalian brains (6–8). Despite the theoretical appeal of Hebb's idea (9) and growing empirical evidence of assemblies (10–12), it remains unclear how diverse groups of neurons spanning several cortical regions transiently coordinate their activity to form cell assemblies or how multiple coactive assemblies regulate their interactions to form larger functional networks.

Brain rhythms may play a key role in coordinating neuronal ensembles (13–15), with a dynamic hierarchy of neuronal oscillations modulating local computation and long-range communication (16–18). This hypothesis is supported by evidence that spiking activity depends on the local field potential (LFP) in both hippocampus (19–21) and neocortex (22, 23). In particular, single-neuron spike timing depends on frequency-specific oscillatory LFP phase, both proximal to the neuron (24) and at more distal locations (25). That is, considering the LFP filtered at a given frequency as a sinusoidal waveform, individual neurons tend to emit spikes clustered around a preferred phase, such as the peak (phase: 0 rad or 0°) or trough (phase: π rad or 180°) of the waveform (Fig. S1). In addition to this dependence upon absolute LFP phase, spiking also depends on LFP–LFP phase coupling between distal and proximal sites (26). LFP–LFP phase coupling is estimated from the distribution of phase differences between two LFP signals (Fig. S2E) and is a measure of the direct dependence between two signals. In other words, given the frequency-specific phase for one LFP signal, how much does one know about the phase of the other? Spike timing thus appears to depend on neuronal oscillations in both proximal and distal sites as well as on the strength of phase coherence between them. This dependence suggests that the spiking of single neurons is influenced by patterned oscillatory activity occurring in multiple interconnected brain areas as well as the neuron's local cortical environment.

Despite the variety of evidence for LFP–neuron interactions, the role of distributed neuronal oscillations in coordinating single-unit and cell assembly activity remains an open question. We therefore investigated the main hypothesis that oscillations enable computation and long-range communication in distributed brain networks, focusing on the relationship between cell assemblies, proximal and distal LFP phases, and LFP–LFP phase coupling. Specifically, our hypotheses were (*i*) that spike timing in single neurons depends on oscillatory phase coupling across multiple brain areas (Fig. 1 *A–D*), (*ii*) that large-scale patterns of phase coupling synchronize anatomically dispersed neuronal ensembles (Fig. 1 *E–G*), and (*iii*) that sensitivity to distinct brain rhythms or coupling patterns permits selective control of multiple coactive assemblies (Fig. 1 *H–J*).

Results

We tested these hypotheses using existing data sets recorded from macaque frontal cortex. Two monkeys engaged in a brain–machine interface (BMI) task (27) had multiple microelectrode arrays chronically implanted bilaterally in primary motor (M1) and dorsal premotor (PMd) cortex. We also examined data from two monkeys performing a working memory task (28) with acute bilateral recordings in multiple prefrontal areas including dorsal and ventral prefrontal cortex (PFdl and PFvl, respectively), orbitofrontal cortex (PFo), and the dorsal bank of the cingulate sulcus (PFcs).
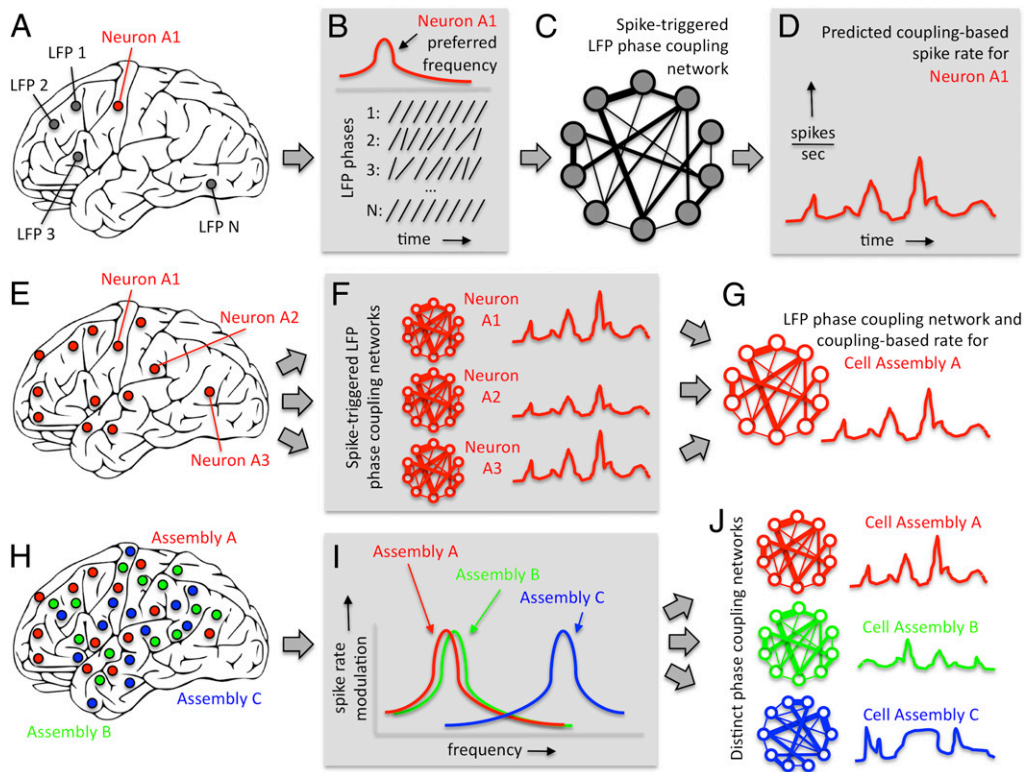
Fig. 1. Patterns of oscillatory phase coupling across multiple brain areas coordinate anatomically dispersed neuronal cell assemblies (schematic). (*A–D*) Hypothesis 1: Spike timing in single neurons depends on frequency-specific oscillatory phase coupling across multiple brain areas. (*A*) Spiking in one area may depend on population activity (local field potentials, LFPs) occurring in multiple areas. (*B*) Many neurons are sensitive to oscillatory LFP activity occurring in particular frequency bands; filtering all LFPs at this frequency and extracting phases can reveal patterns of phase coupling between LFP channels. (*C*) The strength of LFP–LFP phase coupling is different for spike times compared with randomly selected times and defines a neuron's preferred pattern of LFP–LFP phase coupling, similar to a receptive field. That is, when LFP activity matches the neuron's preferred pattern of LFP–LFP phase coupling, the cell spikes more often. (*D*) Given novel LFP phases as input, the model generates a predicted coupling-based spike rate output, which can then be compared with the measured spike rate. (*E–G*) Hypothesis 2: Large-scale patterns of phase coupling synchronize anatomically dispersed neuronal ensembles. (*E*) The procedure described above can be applied to multiple simultaneously recorded neurons. (*F*) Cells that prefer similar LFP–LFP phase-coupling patterns exhibit similar coupling-based rates. (*G*) Shared variability in coupling-based rates is compactly described by a single phase coupling network that defines a cell assembly. That is, it is possible to identify large-scale patterns of LFP–LFP phase coupling (*G*) that explain a significant fraction of the variation in spike rates for a large ensemble of neurons distributed across multiple brain areas. (*H–J*) Hypothesis 3: Differential sensitivity to distinct brain rhythms or coupling patterns permits selective control of multiple coactive assemblies. (*H*) Multiple functional ensembles, each spanning several brain areas, overlap in space. (*I*) Interference between ensembles is minimized when each assembly responds to a different frequency (assemblies A and C) or distinct phase-coupling pattern (assemblies A and B). (*J*) Frequency and pattern selectivity permits dynamic, independent coordination of multiple coactive ensembles.

These data show that neuronal spiking is modulated by widespread LFP activity occurring in distinct frequency bands. In particular, the instantaneous spike rates of most cells are statistically dependent on LFP phases in multiple areas (Fig. S3). Fig. 2*A* shows the dependence of a M1 neuron upon frequency-specific LFP phase in three different brain areas (28 LFP channels in right M1, where the neuron is located; 16 in left M1; and 4 in right PMd). All LFP electrodes were at least 500 μm from the electrode used to record spikes from this neuron, with most electrodes several millimeters away or in the opposite hemisphere. Fig. 2*A* shows the dependence between spike rate and LFP phase as a function of frequency, where the influence of each LFP channel is considered separately. Typical of motor cortical neurons (29), this cell exhibits a strong dependence on the motor high β (25–40 Hz)-band across most electrodes. For example, if we filter the LFP signal recorded from an electrode in left M1 (blue traces in Fig. 2*A*, opposite hemisphere from the neuron), we find that the distribution of all phases over a long time interval is uniform (Fig. S2*B*), but that the distribution of phases that occur at spike times is nonuniform and is clustered around a preferred phase (Fig. S2*C*). This result indicates that spike times and the LFP phase on that channel are statistically dependent and that variation in LFP phase can be converted into

a modulation of the expected neuronal spike rate (*SI Methods*). Given the strong modulation in the high β-band for most recorded neurons (29), for the M1–PMd datasets we therefore focused exclusively on the dependence between spikes and 36-Hz phases.

What are the network origins of this dependence? One possibility is that the spiking of this neuron is directly dependent on the LFP activity occurring in the opposite hemisphere, perhaps mediated by direct synaptic contact of projecting transcallosal axons. Alternatively, the neuron may be directly coupled to the proximal LFP through synaptic connections with local interneurons, but not coupled to distal LFP signals, whereas the LFPs from proximal and distal cortical areas are nonetheless in phase coherence. In the second case, spikes and distal LFP phases would not be dependent once proximal LFP phases were known—spikes and distal LFP phases would be conditionally independent given proximal LFP phase. A similar situation may hold for the spike timing dependence on LFP–LFP phase coupling, where such dependence dissolves once conditioned upon proximal phases.

Critically, we cannot answer this question by examining the dependence of spiking upon each LFP channel separately—such an analysis ignores the influence of LFP–LFP interactions and will therefore generate misleading results. Due to widespread network
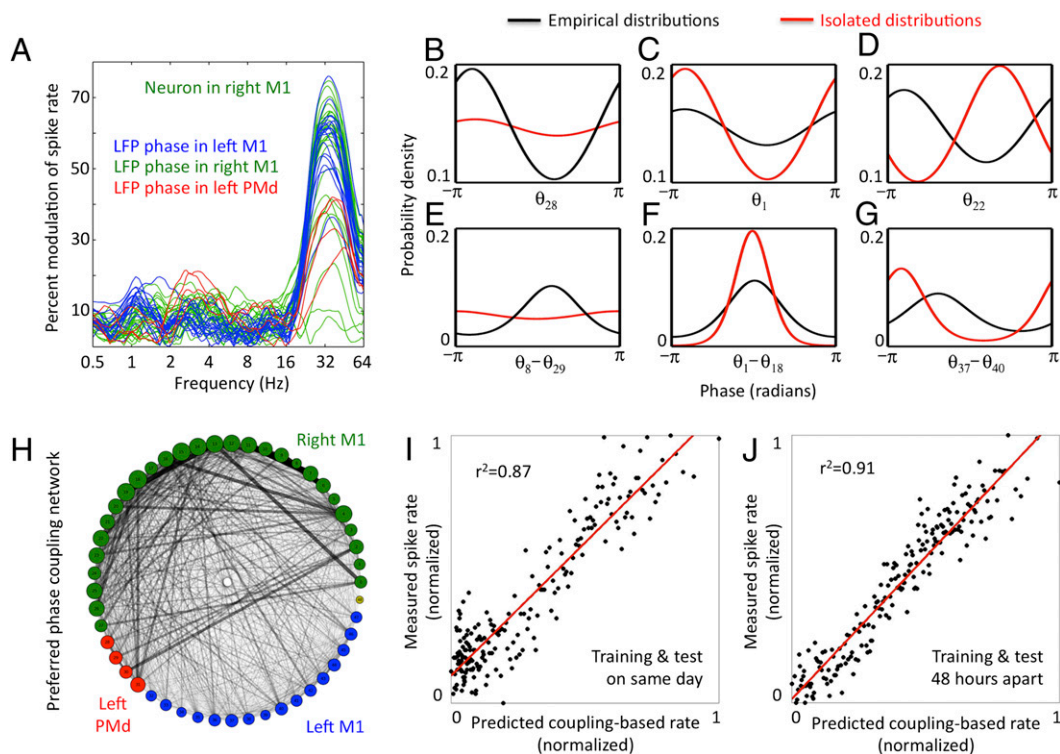
Fig. 2. Spike timing in single neurons depends on oscillatory phase coupling between multiple brain areas. (*A*) Example of a neuron where the probability of spiking depends on frequency-specific LFP phase in multiple areas. The neuron is located in right primary motor cortex (M1). Colored traces represent different LFPs recorded from left M1 (blue), right M1 (green), or left dorsal premotor area (PMd, red). The strong high β (25–40 Hz)-modulation shown here is typical of M1-PMd neurons. (*B–G*) Estimates of spike/LFP interactions depend on the method used and some commonly used techniques may generate misleading results. Examining all LFP signals at once results in differing estimates of phase coupling strength compared with examining pairs of LFP signals separately, as shown by differences between empirical (black) and isolated (red) probability density functions (main text and *SI Methods*; also Figs. S4 and S5). (*H*) Preferred phase coupling network representing 48 LFPs from three brain areas for the M1 neuron shown in *A*. Nodes represent LFP phase variables; links represent the strength of LFP–LFP phase coupling, from weak (light lines) to strong (dark lines). Node size is proportional to the sum of link connection weights entering the node. Strong cross-area coupling remains after conditioning on proximal/distal phases and within-area phase coupling. This preferred pattern of phase coupling acts like an internal, LFP-based receptive field; when the instantaneous pattern of phase coupling between electrodes is close to the preferred coupling pattern, the cell spikes more often. (*I*) The coupling-based spike rate (generated from the preferred LFP–LFP phase coupling pattern learned from training data and instantaneous LFP phases from test data) predicts the measured spike rate (calculated using spike times from test data). (*J*) The relationship between predicted and measured spike rates is stable over multiple days.

connectivity, the phase distribution of one channel, or the distribution of phase differences between two channels, is shaped by the full network of LFP–LFP phase coupling between all channels. We therefore estimated the joint probability distribution over phases using a recently developed multivariate model for circular variables (30) that accounts for these complex network effects (*SI Methods* and Figs. S4 and S5).

Whereas empirical univariate phase distributions are often used to estimate phase concentration and phase coupling, additional influences due to network connectivity bias these estimates. That is, empirical (marginal) probability density functions (PDFs) (black in Fig. 2 *B–G*) differ from the isolated distributions that would be observed if network effects were removed (red in Fig. 2 *B–G*); we term these "isolated distributions," because they single out effects due to coupling between only the phases of interest (*SI Methods*). Isolated distributions provide a more accurate estimate of the direct coupling between two nodes within a larger network than does considering those two nodes alone. For example, Fig. 2*B* shows a case where accounting for network influence reduces our estimate of spike/phase dependence, producing a flatter distribution. In contrast, for some channels removing network effects reveals stronger spike/phase dependence (Fig. 2*C*) or shifts in the preferred phase (Fig. 2*D*). Fig. 2 *E–G* shows similar effects for the phase difference between channels used to estimate the strength of LFP–LFP phase

coupling (see also Figs. S4 and S5 for simulations demonstrating these effects).

Surprisingly, the spiking of a single neuron depends on both distal LFP phases and LFP–LFP phase coupling in addition to the proximal LFP phase recorded near the neuronal cell body (Fig. 2*H* and Fig. S3). This dependence indicates that single-unit spiking is related to large-scale network activity patterns rather than simply reflecting local presynaptic phenomena. Importantly, the pattern of phase coupling estimated using all data (baseline coupling) differs from the pattern of phase coupling inferred using spike times alone (spike-triggered coupling). The ratio of these distributions for a given neuron defines its preferred pattern of phase coupling (Fig. 2*H*) and serves as an "internal" receptive field associated with ongoing brain activity, complementing the traditional, stimulus-related "external" receptive field. Each node in Fig. 2*H* represents one LFP electrode, with links between nodes representing LFP–LFP phase coupling. Line shading indicates the strength of LFP–LFP phase coupling. Note that the preferred pattern for this cell exhibits strong coupling between areas (e.g., right M1 and left PMd, shown as links between green and red nodes) as well as strong intra-area coupling (within right M1, green/green links). Importantly, some LFP pairs exhibited increased phase coupling strength, compared with baseline conditions, whereas other LFP pairs displayed decreased coupling (equivalently, increased coupling at a different phase offset).

Canolty et al.

Given a vector of instantaneous phases observed across electrodes at one moment in time, this preferred coupling pattern can be used to generate a phase-coupling–based spike rate prediction. That is, once the joint distribution between spike times and the filtered LFP signals has been learned, a predicted spike rate can be generated from novel LFP input. We call this spike rate prediction, generated from LFP phases alone without reference to the actual spike times, the coupling-based spike rate. Fig. 2 *I–J* shows how this coupling-based rate compares to the actual spike rate when given novel LFP test data (compare with Fig. S6*A* for a neuron from a different subject). Overall, 71.2% of neurons (107/138 for subject P; 51/84 for subject R) exhibited coupling-based rates significantly correlated to measured rates ($P < 0.05$, corrected for multiple comparisons).

Most neurons exhibited preferred phase coupling patterns involving many electrodes in widely separated cortical areas, without the strong localization one might expect from a modular brain architecture. The broad spatial extent of neuron-specific preferred coupling patterns suggests that neurons in different areas may prefer the same pattern and thus have correlated coupling-based rates (Fig. 3 *A* and *B*). In contrast, two neurons with different preferred patterns may exhibit uncorrelated coupling-based rates, even if they are in close proximity (Fig. 3 *C* and *D*). In fact, within a cortical area the correlation between coupling-based rates is independent of interneuron distance (Fig. 3*E*, not significant). In contrast to distance, similarity of neural function predicts coupling-based rate correlations. That is, we can examine the dependence of neuronal spiking on external factors such as target direction in a center-out BMI task (28) to determine neural function, independent of any internal spike/LFP relationships that may exist. Nevertheless, despite assessing these external and internal dependencies separately, on average two neurons with similar directional tuning exhibit stronger coupling-based rate correlations,

with correlation magnitude dropping as preferred directions diverge (Fig. 3*F*, $P < 0.01$). Importantly, observing two neurons with correlated spike rates alone is not enough to produce this result; neuronal spiking must also be dependent on the same pattern of LFP–LFP phase coupling (*SI Methods*).

Given that large-scale patterns of phase coupling influence the activity of multiple neurons in similar ways, could changes in these coupling patterns be used to modulate the activity of a coordinated cell assembly? And, if so, could multiple, coactive assemblies be modulated independently? Independent components analysis (ICA) of coupling-based rates reveals a small set of signals responsible for most of the predictive efficacy (Fig. 3*G*, red). That is, the coupling-based rate for each neuron—a spike rate prediction generated from the ongoing LFP signals combined with the pattern of phase coupling preferred by that neuron—can be decomposed as a weighted sum of independent (and thus uncorrelated) signals encoding spike rate variations over time. Each ICA component is associated with a distinct LFP phase coupling pattern and contributes to the weighted sums for many different neurons. Importantly, as shown by Fig. 3*G*, a subset of these components explains spike rate changes across a large ensemble of neurons and can be used for ICA-based denoising (*SI Methods*). Supporting the hypothesis that distributed LFP patterns coordinate cell assembly activity, these ICA-denoised coupling-based rates reveal synchronized ensemble activity within subsets of simultaneously recorded neurons. For example, the correlation matrix between denoised coupling-based rates reveals overlapping clusters of neurons with similar activity (Fig. 3*H*; compare with Fig. S6*B*). That is, simultaneously recorded neurons can be sorted such that neurons with similar rank within a list have correlated changes in predicted spike rates. This shared spike rate variation is evidence that large-scale patterns of phase coupling synchronize anatomically dispersed neuronal ensembles.
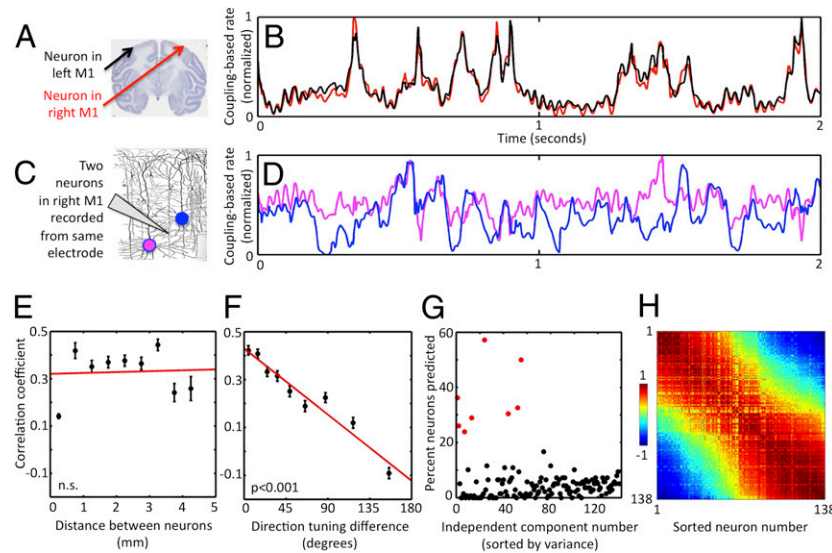

Fig. 3. Large-scale patterns of phase coupling synchronize anatomically dispersed neuronal ensembles. Neurons that prefer similar LFP–LFP phase coupling patterns show correlations between coupling-based spike rates, independent of distance. (*A* and *B*) Two neurons from left and right M1 with correlated coupling-based spike rates. (*C* and *D*) Two neurons recorded from one microelectrode exhibit a weak coupling-based spike rate correlation despite close spatial proximity. (*E*) Within a cortical area, coupling-based spike rate correlations do not depend on interneuron distance (5,716 pairs, n.s.). (*F*) In contrast, motor cortical neurons with similar direction tuning measured during a center-out BMI movement task (28) exhibit coupling-based spike rate correlations (9,413 pairs, $P < 0.001$), suggesting that coupling-based spike rate correlations depend on neural function but not spatial location. (*G*) Shared variability in coupling-based rates is concentrated by independent components analysis (ICA), with a small set of components (red) accounting for most of the predictive value of coupling-based rates (see text). (*H*) Correlation matrix of ICA-denoised coupling-based rates, sorted to identify clusters of neurons with similar activity; e.g., neurons 1–10 form a spatially distributed ensemble with correlated coupling-based rates, have a low correlation with the activity of neurons 61–70, and are anticorrelated with neurons 121–130. The LFP–LFP phase coupling patterns associated with these ICA components explain a portion of the internally generated spike rate variations across an ensemble of anatomically distributed cells and may therefore bind these cells into a functional assembly via Hebbian synaptic modification.

Whereas we have shown that spiking depends on large-scale phase coupling patterns, this dependence may be unrelated to perception, cognition, and action. It is therefore of interest that coupling-based rates exhibit event-related changes during behavior. Monkeys engaged in a BMI task (28) must move a cursor to one of eight targets, and significant changes are seen in the trial average of coupling-based rates locked to the onset of a "go" cue (Fig. 4B, $P < 0.01$, corrected). Furthermore, as shown by Fig. 4 C and D, different cue-locked averages (red) correlate with spike-based peristimulus time histograms (PSTHs) (blue) of specific neurons. This correlation is evidence that the relation of spikes to distributed patterns of LFP phase coupling holds during purposeful behavior as well as spontaneous ongoing activity and can be used to predict event-related changes in neural activity.

Finally, for cell assemblies to be effective, multiple ensembles must be able to act in an independent, multiplexed fashion (Fig. 1H). One potential mechanism was identified above: Distinct phase-coupling patterns at a given frequency can generate independent modulatory signals that drive different sets of neurons (Fig. 1I, cell assemblies A and B, and Fig. 3H). Another possibility is

that different ensembles tune into distinct brain rhythms, a form of frequency–domain modularity (Fig. 1I, assemblies A and C). As in Fig. 2A, Fig. 4 E–H shows prefrontal neurons with distinct frequency preferences across many areas, whereas Fig. 4I shows the sorted optimal frequencies for all 813 frontal neurons examined in this study. Preferred frequencies span a wide range from <0.3 Hz to >40 Hz, such that for any given frequency there exists a large ensemble of neurons modulated by phase coupling patterns occurring at that frequency. Such ensembles experience a common modulatory drive and thus have the potential to operate as a coherent assembly ("fire together, wire together"). Thus, the sensitivity of neurons to (i) distinct brain rhythms as well as (ii) distinct, single-frequency coupling patterns suggests two mechanisms for the selective control of multiple coactive assemblies.

Discussion

Are oscillations simply epiphenomenal reflections of population activity? Or can fluctuations in electric fields have a causal impact on neuronal networks? Recent studies show that externally generated, experimenter-controlled oscillatory electric fields have a causal impact on hippocampal (31) and neocortical (32) slices in vitro. Importantly, the timing of external stimuli relative to the phase of the oscillating field can affect spike probability and timing (31, 32). Other studies used current injection to simulate synaptic input and show that cellular (33) and network (2) properties interact with the injected current to influence spiking timing (34) and stimulus discriminability (35). Finally, in vivo studies show that depth of processing varies with local oscillatory phase (15, 36, 37) and that oscillatory activity arises from interacting networks of multiple cell subtypes (21, 38–40). Thus, neuronal oscillations clearly have a direct causal impact upon local cortical computation.

In contrast to these local effects, oscillations in distant cortical areas cannot have a direct ephaptic (field-only) influence upon neurons. The dependence of spiking on distal phases and phase coupling shown in this study must therefore rely on synaptic connections mediated by projecting axons. Our findings complement Fries' communication through coherence (CTC) hypothesis (14), where relative phase differences modulate the effective connectivity between two cortical areas (26). Our hypothesis that distributed LFP activity influences spiking activity (Fig. 1 A–D) incorporates N distinct phase signals simultaneously and can be considered a natural extension of the inherently two-dimensional CTC hypothesis. That is, we show that spiking in single neurons depends on the full pattern of oscillatory phases occurring in multiple brain areas and that phase coupling patterns will therefore have an impact on long-range communication.

The idea that oscillations also play a key role in perception, cognition, and action is strengthened by findings that oscillations are entrained by early sensory (15), motor (41), and linguistic (42) events. This entrainment depends on attention (15, 41) and provides a link to internal processes critical for learning and memory—processes associated with characteristic low-frequency brain rhythms (13, 43). Prior work suggests a relationship between rhythm frequency and the spatial extent of engaged brain networks, with low frequencies binding large-scale networks and high frequencies coordinating smaller networks (44). It is intriguing to speculate on the connection between the fluid, higher-order cognitive processing enabled by prefrontal areas, on the one hand, and the diversity of prefrontal rhythms that may coordinate multiple cell assemblies, on the other. These connections are beyond the scope of this paper, but could be investigated using a similar methodology.

In agreement with prior studies (45, 46), we show above that neurons are sensitive to multiple frequencies. The cellular and network origins of different rhythms are the focus of ongoing research (39), but the period of concatenation hypothesis (47) provides an elegant mechanism that generates the frequency bands observed in neocortex. Each distinct brain rhythm thus generated could exert independent control of different neuronal ensembles. Furthermore,
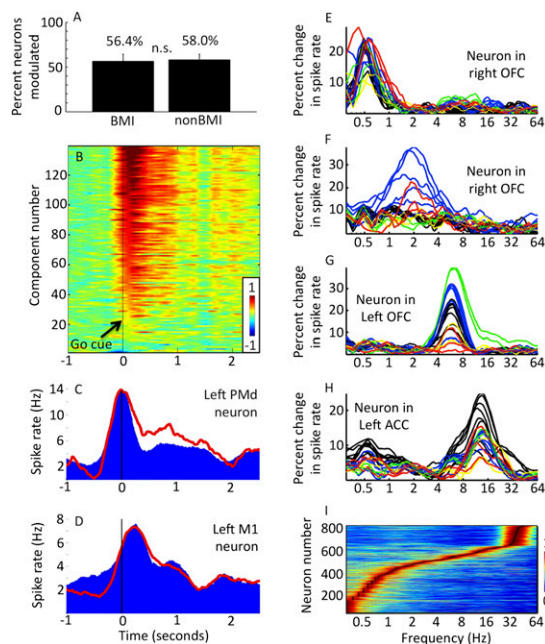

Fig. 4. Phase coupling networks exhibit behavior-related changes and may selectively respond to different frequency bands. (A) Monkeys engaged in a brain–machine interface (BMI) task, using some cells (BMI neurons) to drive an on-screen cursor (28). The percentage of neurons exhibiting significant coupling-based rate modulation was the same for BMI and non-BMI groups. (B) Predicted spike rates generated by assembly-specific coupling patterns (*SI Methods*) show event-related changes. Time is relative to GO cue onset; the vertical axis shows different independent components sorted by activity level 100 ms after cue onset. (C) Peristimulus time histogram (PSTH, blue) for a PMd neuron shows an activity peak at cue onset. The cue-locked average of one coupling-based rate (red) shows event-related changes that correlate with PSTH activity. (D) As in C, for a M1 neuron and different coupling-based rate. Both PSTH (blue) and coupling-based rate (red) peak ~100 ms after cue. (E–H) Different neurons are sensitive to distinct frequencies. Plots show neuronal sensitivity to LFP phase versus frequency (compare with Fig. 2A). Colored traces represent LFPs from different areas: right (red) and left (yellow) dorsolateral prefrontal cortex, right (blue) and left (green) orbitofrontal cortex, and left cingulate sulcus (black). (I) Eight hundred thirteen neurons from four subjects sorted by preferred frequency (black dots). Horizontal lines show normalized modulation strength from low (blue) to high (red) versus frequency; the broad range of preferred frequencies may enable multiple ensembles to operate with minimal interference.

interactions between different frequency bands (16, 17, 48, 49) may provide a mechanism to coordinate the activity of multiple functional assemblies; future research will be required to determine the impact of cross-frequency coupling on spike/LFP interactions.

Here we presented evidence that dynamic patterns of oscillatory coupling across multiple brain areas coordinate anatomically dispersed neuronal cell assemblies. In particular, we found that spike timing depends on distal LFP phases and long-range phase coupling, even after accounting for proximal phase. Different neurons with similar phase-coupling preferences exhibit similar coupling-based rates, independent of interneuron distance. Importantly, this modulation depends on the functional role of neurons and correlates with behavior, suggesting that neuronal oscillations may synchronize anatomically dispersed ensembles actively engaged in functional roles. Finally, we found that frontal neurons are selective for a broad range of frequencies and distinct patterns of phase coupling and thus may provide a mechanism for selective control of multiple coactive assemblies. Together, these findings support the hypothesis that neuronal oscillations play a role in coordinating the functional cell assemblies thought to be responsible for computation and communication in large-scale brain networks.

Methods

A detailed description of the methods is provided in *SI Methods*.

Surgery, Electrophysiology, and Analysis. Two adult monkeys were chronically implanted with multiple microelectrode arrays bilaterally in M1 and PMd and performed a BMI task. Two different monkeys engaged in a working memory task and had acute recordings made from multiple prefrontal areas. The pairwise phase distribution of LFP measurements was modeled using a probabilistic model (30). For each neuron, two models were fitted using either all LFP data or LFP phases occurring at spike times alone and then related using Bayes' rule.

1. Kandel E (2000) *Principles of Neural Science* (McGraw–Hill, New York), 4th Ed.
2. Destexhe A, Rudolph M, Paré D (2003) The high-conductance state of neocortical neurons in vivo. *Nat Rev Neurosci* 4:739–751.
3. Shepherd GM, Stepanyants A, Bureau I, Chklovskii D, Svoboda K (2005) Geometric and functional organization of cortical circuits. *Nat Neurosci* 8:782–790.
4. Douglas RJ, Martin KAC (2004) Neuronal circuits of the neocortex. *Annu Rev Neurosci* 27:419–451.
5. Hebb DO (1949) *The Organization of Behavior* (Wiley, New York).
6. Varela F, Lachaux JP, Rodriguez E, Martinerie J (2001) The brainweb: Phase synchronization and large-scale integration. *Nat Rev Neurosci* 2:229–239.
7. Greicius MD, Krasnow B, Reiss AL, Menon V (2003) Functional connectivity in the resting brain: A network analysis of the default mode hypothesis. *Proc Natl Acad Sci USA* 100:253–258.
8. Mesulam MM (1990) Large-scale neurocognitive networks and distributed processing for attention, language, and memory. *Ann Neurol* 28:597–613.
9. Harris KD (2005) Neural signatures of cell assembly organization. *Nat Rev Neurosci* 6:399–407.
10. Harris KD, Csicsvari J, Hirase H, Dragoi G, Buzsáki G (2003) Organization of cell assemblies in the hippocampus. *Nature* 424:552–556.
11. Riehle A, Grün S, Diesmann M, Aertsen A (1997) Spike synchronization and rate modulation differentially involved in motor cortical function. *Science* 278:1950–1953.
12. Hoffman KL, McNaughton BL (2002) Coordinated reactivation of distributed memory traces in primate neocortex. *Science* 297:2070–2073.
13. Miller R (1991) *Cortico-Hippocampal Interplay and the Representation of Contexts in the Brain* (Springer, New York).
14. Fries P (2005) A mechanism for cognitive dynamics: Neuronal communication through neuronal coherence. *Trends Cogn Sci* 9:474–480.
15. Lakatos P, Karmos G, Mehta AD, Ulbert I, Schroeder CE (2008) Entrainment of neuronal oscillations as a mechanism of attentional selection. *Science* 320:110–113.
16. Lakatos P, et al. (2005) An oscillatory hierarchy controlling neuronal excitability and stimulus processing in the auditory cortex. *J Neurophysiol* 94:1904–1911.
17. Canolty RT, et al. (2006) High gamma power is phase-locked to theta oscillations in human neocortex. *Science* 313:1626–1628.
18. Canolty RT, et al. (2007) Spatiotemporal dynamics of word processing in the human brain. *Front Neurosci* 1:185–196.
19. Bragin A, et al. (1995) Gamma (40-100 Hz) oscillation in the hippocampus of the behaving rat. *J Neurosci* 15:47–60.
20. Chrobak JJ, Buzsáki G (1998) Gamma oscillations in the entorhinal cortex of the freely behaving rat. *J Neurosci* 18:388–398.
21. Klausberger T, et al. (2004) Spike timing of dendrite-targeting bistratified cells during hippocampal network oscillations in vivo. *Nat Neurosci* 7:41–47.
22. Freeman WJ (1975) *Mass Action in the Nervous System* (Academic, New York).
23. Eeckman FH, Freeman WJ (1990) Correlations between unit firing and EEG in the rat olfactory system. *Brain Res* 528:238–244.
24. Jacobs J, Kahana MJ, Ekstrom AD, Fried I (2007) Brain oscillations control timing of single-neuron activity in humans. *J Neurosci* 27:3839–3844.
25. Siapas AG, Lubenov EV, Wilson MA (2005) Prefrontal phase locking to hippocampal theta oscillations. *Neuron* 46:141–151.
26. Womelsdorf T, et al. (2007) Modulation of neuronal interactions through neuronal synchronization. *Science* 316:1609–1612.
27. Ganguly K, Carmena JM (2009) Emergence of a stable cortical map for neuroprosthetic control. *PLoS Biol* 7:e1000153.
28. Kennerley SW, Wallis JD (2009) Reward-dependent modulation of working memory in lateral prefrontal cortex. *J Neurosci* 29:3259–3270.
29. Rubino D, Robbins KA, Hatsopoulos NG (2006) Propagating waves mediate information transfer in the motor cortex. *Nat Neurosci* 9:1549–1557.
30. Cadieu CF, Koepsell K (2010) Phase coupling estimation from multivariate phase statistics. *Neural Comput*, in press. Available at: http://redwood.berkeley.edu/klab/papers/CadieuKoepsell_PCE_NeuralComp.pdf.
31. Fujisawa S, Matsuki N, Ikegaya Y (2004) Chronometric readout from a memory trace: Gamma-frequency field stimulation recruits timed recurrent activity in the rat CA3 network. *J Physiol* 561:123–131.
32. Fröhlich F, McCormick DA (2010) Endogenous electric fields may guide neocortical network activity. *Neuron* 67:129–143.
33. Hutcheon B, Yarom Y (2000) Resonance, oscillation and the intrinsic frequency preferences of neurons. *Trends Neurosci* 23:216–222.
34. Volgushev M, Chistiakova M, Singer W (1998) Modification of discharge patterns of neocortical neurons by induced oscillations of the membrane potential. *Neuroscience* 83:15–25.
35. Schaefer AT, Angelo K, Spors H, Margrie TW (2006) Neuronal oscillations enhance stimulus discrimination by ensuring action potential precision. *PLoS Biol* 4:e163.
36. Kruglikov SY, Schiff SJ (2003) Interplay of electroencephalogram phase and auditory-evoked neural activity. *J Neurosci* 23:10122–10127.
37. Koepsell K, Wang X, Hirsch JA, Sommer FT (2010) Exploring the function of neural oscillations in early sensory systems. *Front Neurosci* 4:53–61.
38. Mitzdorf U (1985) Current source-density method and application in cat cerebral cortex: Investigation of evoked potentials and EEG phenomena. *Physiol Rev* 65:37–100.
39. Traub RD, Bibbig A, LeBeau FEN, Buhl EH, Whittington MA (2004) Cellular mechanisms of neuronal population oscillations in the hippocampus in vitro. *Annu Rev Neurosci* 27:247–278.
40. Cardin JA, et al. (2009) Driving fast-spiking cells induces gamma rhythm and controls sensory responses. *Nature* 459:663–667.
41. Saleh M, Reimer J, Penn R, Ojakangas CL, Hatsopoulos NG (2010) Fast and slow oscillations in human primary motor cortex predict oncoming behaviorally relevant cues. *Neuron* 65:461–471.
42. Luo H, Poeppel D (2007) Phase patterns of neuronal responses reliably discriminate speech in human auditory cortex. *Neuron* 54:1001–1010.
43. Rizzuto DS, Madsen JR, Bromfield EB, Schulze-Bonhage A, Kahana MJ (2006) Human neocortical oscillations exhibit theta phase differences between encoding and retrieval. *Neuroimage* 31:1352–1358.
44. von Stein A, Sarnthein J (2000) Different frequencies for different scales of cortical integration: From local gamma to long range alpha/theta synchronization. *Int J Psychophysiol* 38:301–313.
45. Whittington MA, Traub RD (2003) Interneuron diversity series: Inhibitory interneurons and network oscillations in vitro. *Trends Neurosci* 26:676–682.
46. Jacobs J, Kahana MJ, Ekstrom AD, Fried I (2007) Brain oscillations control timing of single-neuron activity in humans. *J Neurosci* 27:3839–3844.
47. Kramer MA, et al. (2008) Rhythm generation through period concatenation in rat somatosensory cortex. *PLoS Comput Biol* 4:e1000169.
48. Tort ABL, et al. (2008) Dynamic cross-frequency couplings of local field potential oscillations in rat striatum and hippocampus during performance of a T-maze task. *Proc Natl Acad Sci USA* 105:20517–20522.
49. Tort ABL, Komorowski RW, Manns JR, Kopell NJ, Eichenbaum H (2009) Theta-gamma coupling increases during the learning of item-context associations. *Proc Natl Acad Sci USA* 106:20942–20947.

NEUROSCIENCE

APPLIED PHYSICAL SCIENCES

Supporting Information

Canolty et al. 10.1073/pnas.1008306107

SI Methods

1. Surgery, Electrophysiology, and Experimental Setup for the Brain–Machine Interface Task. See ref. 1 for full experimental details. Two adult male rhesus monkeys (*Macaca mulatta*) were chronically implanted with multiple microelectrode arrays. Each array consisted of 64 Teflon-coated tungsten microelectrodes (35 μm in diameter, 500-μm interelectrode spacing) arranged in an 8 × 8 array (CD Neural Engineering). Subject P was implanted bilaterally in the arm area of primary motor cortex (M1) and in the arm area of left hemisphere dorsal premotor cortex (PMd), for a total of 192 electrodes across three implants. One hundred thirty-eight identified single units from this subject were examined. Subject R had bilateral implants in the arm area of M1 and PMd, for a total of 256 electrodes across four implants. Eighty-four identified single units from this subject were examined. Localization was performed using stereotactic coordinates (2). Implants targeted layer-5 pyramidal tract neurons and were positioned at a depth of 3 mm (M1) or 2.5 mm (PMd). Intraoperative monitoring of spike activity guided electrode depth. Conducted procedures were in compliance with the National Institutes of Health Guide for the Care and Use of Laboratory Animals and approved by the University of California (Berkeley) Institutional Animal Care and Use Committee.

The MAP system (Plexon) was used to record unit activity. Only single units that had a clearly identified waveform with a signal-to-noise ratio of at least 4:1 were used. An on-line spike-sorting application (Sort-Client; Plexon) was used to sort activity before recording sessions. Large populations of well-isolated units and up to 128 LFP channels (1 kHz sampling) were recorded during daily sessions for both monkeys.

Monkeys were trained to perform a center-out delayed reaching task using a Kinarm (BKIN Technologies) exoskeleton (manual control) as well as a brain–machine interface task where a cursor was controlled by neural activity (brain control). During training and recording, animals sat in a primate chair that permits limb movements and postural adjustments. Head restraint consisted of the animal's headpost fixated to a primate chair. Recording sessions typically lasted 2–3 h/d. Because of their longer session duration, only brain control sessions are discussed in this paper. During brain control sessions a visually presented cursor was continuously controlled by neural activity while both hands were restrained. Subjects self-initiated trials by bringing the cursor to the center for a hold period of 250–300 ms, followed by the presentation of a GO cue (color change of center cue). A trial error occurred if the cursor failed to reach the target within 10 s after a GO cue. The goal was to perform a center-out task, moving the cursor from the center to one of eight peripheral targets distributed over a 14-cm–diameter circle. Target radius was typically 0.75 cm. A liquid reward was provided after a successful reach to each target.

For all sessions for subject P, from the 192 implanted electrodes, 128 LFP channels recorded, with >160 distinct units identified via automatic spike sorting. Only cells with a spike rate >1 Hz were examined. Different figures display results from different numbers of neurons from distinct sessions: specifically, Fig. 2, 1 neuron from session paco020608c; Fig. 3 *B* and *D*, 4 neurons from session paco020608c; Fig. 3 *E–H*, 138 neurons from session paco020608c; Fig. 4*A*, 138 neurons from sessions paco020608b, -c, and -d; Fig. 4*B*, 138 neurons from all sessions; Fig. 4*C*, 1 neuron from session paco020608c; Fig. 4*D*, 1 neuron from session paco020608c; Fig. 4*I*, 138 neurons from session paco020608c; Fig. S2 *A–C*, 1 neuron from session paco020608b; Fig. S3, 138 neurons from session paco020608c.

2. Surgery, Electrophysiology, and Experimental Setup for the Working Memory Task. See ref. 3 for full experimental details. Two male rhesus monkeys (*M. mulatta*, subjects A and B) were implanted with head positioners and two recording chambers, the positions of which were determined using a 1.5-T magnetic resonance imaging (MRI) scanner. Acute simultaneous recordings were made using arrays of 10–24 tungsten microelectrodes (FHC Instruments). Over several days, recordings were made in dorsolateral prefrontal cortex (DLPFC), ventrolateral prefrontal cortex (VLPFC), orbitofrontal cortex (OFC), and anterior cingulate cortex (ACC). Target electrode positions were determined from MRI images and electrodes were advanced using custom-built, manual microdrives until they were located just above the cell layer. Electrodes were slowly lowered into the cell layer until neuronal waveforms were obtained. Neurons were randomly sampled with no attempt made to select neurons on the basis of responsiveness. Waveforms were digitized and analyzed off-line (Plexon). Recording locations were reconstructed by measuring recording chamber position using stereotactic methods, with the correspondence between MRI sections and recording chambers confirmed by mapping the position of sulci and gray and white matter boundaries using neurophysiological recordings. The distance of each recording location along the cortical surface, from the genu of the ventral bank of the principal sulcus and the lateral surface of the inferior convexity, was traced and measured, as were the positions of the other sulci relative to the principal sulcus. All procedures were in accord with the National Institutes of Health guidelines and the recommendations of the University of California (Berkeley) Animal Care and Use Committee.

Subjects engaged in a task targeting reward-dependent modulation of working memory. National Institute of Mental Health Cortex was used to control the stimulus presentation and task contingencies. Eye position and pupil dilation were monitored using an infrared system at 125 Hz sampling rate (ISCAN). Trials began with subjects fixating a central square cue (subtending 0.3° of visual angle). Subjects maintained fixation within 2° of the fixation cue throughout the trial until the fixation cue changed color, after which subjects made their response. Failure to maintain fixation resulted in a 5-s "time out" and trial abortion. Following fixation, two cues appeared sequentially and separated by a delay, one of which was a spatial location that the subject had to hold in working memory (the mnemonic stimulus), and one of which indicated to the subject how much reward they would receive for performing the task correctly (the reward-predictive cue). Following a second delay a fixation-cue color change indicated that subjects could saccade to the location of the mnemonic stimulus. Once subjects made eye movements indicating their response, they had 400 ms to saccade within 3° of the target location. Successful target saccades with 400 ms were followed by a fixation hold of 150 ms. Failures to saccade to the target within 400 ms or fixate the target for 150 ms were classified as trial errors and terminated the trial without delivery of reward. Twenty-four locations forming a 5 × 5 matrix centered at fixation (each location separated by 4.5°) were used as spatial targets. There were five different reward sizes. Each reward amount was represented by one of two pictures. All experimental factors were fully counterbalanced, and different trial types were randomly intermingled. Subjects completed ≈600 correct trials per day.

Different figures display results from different numbers of neurons from distinct sessions: specifically, Fig. 4*I*, 329 neurons from all sessions from subject A and 262 neurons from all sessions from subject B.

3. Analysis: LFP Filtering and Phase Extraction. Analyses were done using MATLAB (Mathworks) or Python. All filtering was done using Gaussian chirplet basis functions (4). A Gaussian chirplet is fully defined by four parameters: namely, the center time t_0, the center frequency v_0, the duration parameter s_0, and the chirp rate c_0 (5). In the time domain, the chirplet g is given as $g(t\,|\,t_0, v_0, s_0, c_0) = 2^{1/4}exp[(-1/4)s_0 - \pi(t - t_0)^2exp[-s_0] + \pi(t - t_0)(c_0(t - t_0) + 2v_0)]$. Although informal investigation suggests that it is worthwhile to optimize the parameter set (center frequency, duration parameter, chirp rate) for each neuron separately, for simplicity and ease of comparison in this study we use a fixed chirp rate of 0 Hz/s (no chirping) and a fixed fractional bandwidth (FWHM/center frequency) of 0.325. A constant fractional bandwidth means that chirplets with higher center frequencies have wider frequency-domain passbands, as in the wavelet transform. To extract local field potential (LFP) phases, first the raw LFP signal $x_{\text{RAW}}(t)$ for a given channel was convolved with a complex-valued Gaussian chirplet basis function $g(t)$ to generate a complex-valued time series, which has the same number of sample points N_{time} as the raw LFP signal. The complex angle of this time series defines a $1 \times N_{\text{time}}$ time series of phase variables $\theta(t)$. This process was repeated for all N_{channel} simultaneously recorded LFP signals to generate a multivariate $N_{\text{channel}} \times N_{\text{time}}$ time series of phase variables $\theta(t)$.

4. Analysis: Multivariate Phase Model. To model the pairwise phase distribution of LFP measurements we used a recently derived model and estimation technique of coupled oscillator systems (6). The model specifies a probability distribution, which corresponds to the maximum entropy distribution given pairwise phase measurements. Furthermore, it can be shown that the probabilistic model implies an underlying dynamical system of coupled oscillators and the parameters of the probability distribution are the interactions between the oscillators (6). Therefore, the parameters of the probability model can be interpreted as the interaction strengths between coupled oscillators.

In this section we derive the estimator for the pairwise phase distribution given phase measurements. We then show that a specific dynamical system formulation of coupled oscillators leads to the same pairwise phase distribution and that estimating the probability distribution recovers the interactions of the coupled oscillators. We then describe how the observed empirical distribution of two oscillators relates to the direct interaction (or isolated distribution) between the oscillators and the indirect interaction (or network distribution). Finally, we provide a series of examples to illustrate potential differences between the measured empirical distribution and the true coupling interaction and show how properly estimating the distribution correctly infers the true interaction.

4.1. Pairwise maximum entropy phase distribution. Here we derive the maximum entropy phase distribution given pairwise phase statistics. This distribution allows us to evaluate the phase coupling patterns conditioned on spikes and thus the relationship between spikes and the recorded LFP phases in multiple areas.

Given a set of measurements (i.e., pairwise phase statistics), there is a unique maximum entropy distribution that reproduces the statistics of these measurements. A number of maximum entropy distributions are used throughout the science and engineering communities. In the real-valued case the multivariate Gaussian distribution and in the binary case the Ising model serve as widely used multivariate maximum entropy distributions consistent with second-order statistics. For multivariate phases, the first circular moment is a measurement between two phases, k and l, and is defined as the complex quantity $\langle e^{\mathbf{i}(\theta_k - \theta_l)} \rangle$. The real and imaginary parts are given as

$$\text{Re}\left[\left\langle e^{i(\theta_k - \theta_l)} \right\rangle\right] = \langle\cos(\theta_k - \theta_l)\rangle$$
$$= \langle\cos(\theta_k)\cos(\theta_l) + \sin(\theta_k)\sin(\theta_l)\rangle$$
$$\text{Im}\left[\left\langle e^{i(\theta_k - \theta_l)} \right\rangle\right] = \langle\sin(\theta_k - \theta_l)\rangle$$
$$= \langle\sin(\theta_k)\cos(\theta_l) - \cos(\theta_k)\sin(\theta_l)\rangle$$

Written in this way, the statistical measurements for the first circular moment contain bivariate terms between pairs of phases and are thus second-order phase statistics. Given these statistics it follows that the corresponding maximum entropy distribution is given as

$$p(\theta; \mathbf{K}) = \frac{1}{Z(\mathbf{K})} \exp\left[-\frac{1}{2} \sum_{i,j=1}^{d} \kappa_{ij} \cos(\theta_i - \theta_j - \mu_{ij})\right], \qquad \textbf{[S1]}$$

where θ is the d-dimensional set of phases and $\mathbf{K}$ specifies the parameters of the distribution. We used trigonometric identities to combine the sine and the cosine of the differences of the phase pairs into one term for each pair of phases. The terms κ_{ij} and μ_{ij} are the coupling between phases i and j and the phase offset between phases i and j, respectively. The term $Z(\mathbf{K})$ is the normalization constant and is dependent on the parameters of the distribution. Next we derive an estimator for this distribution: a method for determining the parameters $\mathbf{K}$ from phase measurements.

Given phases from N_{channel} different LFP channels, we can estimate the probability of observing a particular N-dimensional vector of phases using a multivariate phase distribution. An equivalent but more compact expression for the probability distribution given in Eq. **S1** is

$$p(\theta; \mathbf{K}) = \frac{1}{Z(\mathbf{K})} \exp[-E(\theta; \mathbf{K})]$$
$$E(\theta; \mathbf{K}) = \frac{1}{2}\mathbf{z}^*\mathbf{K}\mathbf{z}, \qquad \textbf{[S2]}$$

where we define the N-dimensional vector of phase variables as a vector of unit length complex variables, z_k, where $z_k = \exp(i\theta_k)$ and θ_k is an element of the real-valued interval $[-\pi, \pi]$. The $N_{\text{channel}} \times N_{\text{channel}}$ coupling matrix $\mathbf{K}$ is Hermitian and traceless. The elements of $\mathbf{K}$ encode the coupling parameters between channels; e.g., $\mathbf{K}_{ij}$ encodes the coupling between the ith and jth phase variables. Each element of $\mathbf{K}$ is a complex number $\mathbf{K}_{ij} = \kappa_{ij}\exp(i\mu_{ij})$, where the modulus κ_{ij} encodes coupling strength and the angle μ_{ij} denotes the preferred phase offset between channels. The diagonal elements of $\mathbf{K}$ are zero ($\mathbf{K}_{ii} = 0$), but non-uniform univariate phase distributions can be modeled by augmenting the observed matrix of phase variables with an additional variable of fixed phase, resulting in a $(N_{\text{channel}} + 1) \times (N_{\text{channel}} + 1)$ coupling matrix $\mathbf{K}$. The normalization constant $Z(\mathbf{K})$ is a function of the coupling matrix and in general cannot be computed analytically. Note that Eqs. **S1** and **S2** are equivalent but Eq. **S2** uses complex notation.

Given an observed set of phase variables, we then estimate the parameters of the distribution using an efficient technique derived in ref. 6. The lack of a closed form to the partition function $Z(\mathbf{K})$ makes standard maximum-likelihood estimators computationally expensive and prone to convergence problems. The estimator derived in ref. 6 is a linear system of equations using the measurements of the phase variables. The estimated coupling terms, elements of the matrix $\mathbf{K}$, are found by solving the linear system of equations

$$\sum_{k,l=1}^{d} \left(\delta_{jl}C_{ik} + \delta_{ik}C_{lj} - \delta_{jk}C_{iljk} - \delta_{il}C_{iljk}\right)\widehat{K}_{kl} = 4C_{ij}, \qquad \textbf{[S3]}$$

where the expectation values are defined as $C_{ij} = \langle z_i z_j^* \rangle$ and $C_{ijkl} = \langle z_i z_j z_k^* z_l^* \rangle$. Because the diagonal elements of $\mathbf{K}$ are zero, we can remove the corresponding equations where $i = j$ from the system. We solved this linear system of equations using

standard techniques. This estimator has been shown to correspond to the maximum-likelihood estimate and performs well in high dimensions and with limited data (6). Code to estimate the distribution is available at ref. 7.

In summary, the pairwise phase distribution in Eq. **S1** provides the most parsimonious statistical model of the joint multivariate phase distribution given only pairwise phase measurements. The corresponding estimator in Eq. **S3** provides the unique maximum entropy solution. Maximum entropy solutions serve as the least biased estimate of the distribution possible and can be used when the true joint distribution is unknown.

4.2. Pairwise phase distribution and models of coupled oscillators. In this section we show that the parameters of the phase distribution have a physical interpretation in a dynamic system of coupled oscillators and interestingly, the parameters in the phase distribution are identical to the interactions between the oscillators. We can derive the multivariate phase distribution from a dynamical systems model of coupled oscillators. Given the dynamical system,

$$\frac{\partial}{\partial t}\theta_i(t) = \omega - \sum_{j=1}^{d} \kappa_{ij} \sin\left(\theta_i(t) - \theta_j(t) - \mu_{ij}\right) + v_i(t),$$

a corresponding steady-state distribution can be derived using a suitable Langevin equation. The probability distribution for the phases of this coupled oscillator system is identical to that given above in Eqs. **S1** and **S2**, save for the introduction of a parameter β within the exponential to account for the variance of the noise terms $v_i(t)$. Thus the parameters of the matrix **K** estimated from observed phase data may be interpreted as the interaction terms between a physical system of coupled oscillators.

4.3. Phase-locking value, phase concentration, and phase coupling. In this section we show the relationship between the commonly used phase-locking value, the measured phase concentrations, and the phase coupling parameters in the probability distribution. Importantly, the phase-locking value and the phase concentration are only indirectly related to the phase coupling parameters.

The phase-locking value (PLV) (8) is the amplitude of the first circular moment of the measured phase difference between two phases,

$$PLV := \left| \left\langle e^{\mathbf{i}(\theta_k - \theta_l)} \right\rangle \right|, \qquad \textbf{[S4]}$$

with the expectation $\langle . \rangle$ taken over the phase measurements, and $|x|$ is the complex modulus or amplitude of the complex value x. We can see the relationship between the phase-locking value and the coupling parameters, i.e., κ_{kl}, in the probability distribution by examining the marginal distribution of phase differences. The marginal distribution is defined as

$$p(\theta_k - \theta_l; \mathbf{K}) \sim \int \prod_{i,j=1}^{d} \exp\left[\frac{1}{2}\kappa_{ij}\cos(\theta_i - \theta_j - \mu_{ij})\right] d\theta^{d-2}, \qquad \textbf{[S5]}$$

in which the integration is over all phases θ_m with $m \neq k, l$, which can be either the first or the second variable in the cosine. After applying the variable substitution $\theta_m = \tilde{\theta}_m + \theta_l$, all terms in Eq. **S5** either depend on the phase difference $\theta_k - \theta_l$ or are independent of θ_k and θ_l. The independent terms integrate to a constant and the remaining terms combine to a von Mises distribution in the pairwise phase difference given by

$$p(\theta_k - \theta_l; \mathbf{K}) = \frac{1}{Z(\gamma_{kl})}e^{\gamma_{kl}\cos(\theta_k - \theta_l - \Delta_{kl})}, \qquad \textbf{[S6]}$$

with mean phase Δ_{kl} and concentration parameter γ_{kl}. We call the concentration parameter γ_{kl} for a pair of phases the *phase concentration*. The parameters of the distribution in Eq. **S6** can be estimated from the *first circular moment* $\langle e^{i(\theta_k - \theta_l)} \rangle =: r_{kl}e^{i\Delta_{kl}}$:

the mean phase Δ_{kl} is the complex angle of the first moment and the concentration parameter γ_{kl} can be obtained by numerically solving the equation

$$r_{kl} = I_1(\gamma_{kl})/I_0(\gamma_{kl}), \qquad \textbf{[S7]}$$

and the normalization constant $Z(\gamma_{kl})$ is given by $Z(\gamma_{kl}) = 2\pi I_0(\gamma_{kl})$. $I_0(x)$ and $I_1(x)$ denote the modified Bessel functions of zeroth and first order, respectively. Note that PLV = r_{kl}. The value of γ_{kl} is related to the coupling parameters **K** through Eq. **S5** and thus PLV is related to the coupling parameters through Eqs. **S5**–**S7**. Therefore, there is a nontrivial relationship between the phase-locking value or the measured phase concentrations and the coupling parameters.

Under the dynamical system interpretation of the probability distribution, the interaction between two oscillators i and j is given by the coupling parameters k_{ij} and μ_{ij}. In general there is no simple relationship between these coupling parameters and the measured phase-locking value or phase concentration. However, by properly estimating the coupling parameters from the measurements (*SI Methods 4.1*), we can infer the direct interactions between the oscillators.

4.4. Empirical, isolated, and network distributions. We next show the relationship between the measured empirical distribution, the isolated distribution, and the network distribution. Given a set of phase measurements, we can directly compute the marginal distribution of the phase difference between a specific pair of phases. We call the marginal distribution computed from the difference of phase measurements of θ_k and θ_l the *empirical distribution $p(\theta_k - \theta_l)$*. In a network of many oscillators the empirical distribution is determined by a direct interaction between nodes k and l and an indirect interaction through the rest of the network. Given the probabilistic model in *SI Methods 4.1*, we next show how the empirical distribution can be decomposed into an *isolated distribution*, which captures the direct interaction, and a *network distribution*, which captures the interaction through the network.

For a given set of oscillators and coupling parameters the empirical distribution is given as

$$p(\theta_k - \theta_l; \mathbf{K}) \sim \int \prod_{\{i,j\}} e^{\kappa_{ij}\cos(\theta_i - \theta_j - \mu_{ij})} d\theta^{d-2},$$

which is a reformulation of Eq. **S2** but with the product containing only one term for each pair of oscillators. The integration is over all phases θ_i with $I \neq k, l$. Because the integration is over all phases not equal to k or l, we can factor out the terms containing the coupling parameters between k and l:

$$p(\theta_k - \theta_l; \mathbf{K}) \sim e^{\kappa_{kl}\cos(\theta_k - \theta_l - \mu_{kl})} \int \prod_{\{i,j\} \neq \{k,l\}} e^{\kappa_{ij}\cos(\theta_i - \theta_j - \mu_{ij})} d\theta^{d-2}. \qquad \textbf{[S8]}$$

We can apply the variable substitution $\theta_m = \tilde{\theta}_m + \theta_l$ and all terms in Eq. **S8** either depend on the phase difference $\theta_k - \theta_l$ or are independent of θ_k and θ_l. The independent terms integrate to a constant and the remaining terms combine to a von Mises distribution in the pairwise phase difference. We can therefore decompose the empirical distribution into a product of two von Mises distributions,

$$p(\theta_k - \theta_l; \mathbf{K}) = p_{iso}(\theta_k - \theta_l; \kappa_{kl}, \mu_{kl}) \, p_{net}(\theta_k - \theta_l; \bar{\mathbf{K}}_{kl})$$

$$p_{iso}(\theta_k - \theta_l; \kappa_{kl}, \mu_{kl}) = e^{\kappa_{kl}\cos(\theta_k - \theta_l - \mu_{kl})}$$

$$p_{net}(\theta_k - \theta_l; \bar{\mathbf{K}}_{kl}) = e^{\bar{\kappa}_{kl}\cos(\theta_k - \theta_l - \bar{\mu}_{kl})},$$

where $\bar{\mathbf{K}}_{kl}$ is the set of parameters excluding the direct coupling parameters κ_{kl} and μ_{kl} and the concentration $\bar{\kappa}_{kl}$ and

phase offset $\bar{\mu}_{kl}$ are determined through the integral in Eq. **S8** and depend on all of the parameters $\mathbf{K}_{kl}$ excluding κ_{kl} and μ_{kl}. We refer to the distribution that contains the direct coupling parameters as the *isolated distribution* because it is the distribution that would be measured if only the direct interaction were present and there was no interaction due to the network (the two nodes would be isolated from the rest of the system). We refer to the distribution that contains the network effects on the empirical distribution as the *network distribution* because it is the distribution that would be measured if there were no direct interaction between the nodes and only the interaction through the network was present.

4.5. Example phase-coupled systems and their estimation. In this section we illustrate the differences between phase concentration and estimated phase coupling using a series of simple networks. We also present a more complicated network that shows that the method generalizes to complex networks of interactions.

In Fig. S4 we illustrate three simple networks, their phase concentrations, and estimated phase couplings. For each network we simulated the dynamic system described in *SI Methods 4.2*. We then measured the phase concentration between the indicated pair of oscillators (A and B). We also estimated the coupling parameters using Eq. **S3**. Each network illustrates a specific effect that can be found in the experimental data we examined: *spurious coupling*, *missing coupling*, and *incorrect phase offset*. In each case, phase concentration does not reflect the true direct interaction between the indicated oscillators. Inferring the parameters of the full probabilistic distribution correctly recovers the true coupling between the indicated oscillators and all other pairs. In the last column in Fig. S4 we illustrate the empirical distribution and the isolated distribution (similar to Fig. 2 *B–G*).

In Fig. S5 we present a more complex case of eight coupled oscillators. Again, phase concentrations poorly reflect the direct interactions between oscillators whereas phase coupling estimation correctly infers the true interactions. For a more rigorous analysis of the model estimation performance and behavior of phase coupling estimation see ref. 6.

5. Analysis: Baseline, Spike-Triggered, and Preferred Phase Coupling Patterns and the Generation of Coupling-Based Rates from Phase Data. The previous section (*SI Methods 4*) describes how multichannel LFP data observed during experiments can be used to estimate the coupling within a network of distinct brain areas. How can this information be used to predict the spiking activity of a single neuron? Because the multivariate phase model specifies a joint distribution over the phase variables, we can apply Bayes' rule to determine the probability of a spike conditioned on the state of the multivariate phase up to a normalization constant. Specifically, we can estimate the prior probability of the multivariate phase $p(\boldsymbol{\theta})$ and the conditional probability of the multivariate phase given a neural spike $p(\boldsymbol{\theta}|spike)$. We then apply Bayes' rule to arrive at an estimate of the probability of a spike given a measured multivariate phase state:

$$p(spike|\boldsymbol{\theta}) = \frac{p(\boldsymbol{\theta}|spike)\,p\,(spike)}{p(\boldsymbol{\theta})}.$$

Inserting the equations for the multivariate phase distributions, we find

$$p(spike|\boldsymbol{\theta}) \propto \frac{\exp\left(-\frac{1}{2}\mathbf{z}^*\mathbf{K}_{spike}\mathbf{z}\right)}{\exp\left(-\frac{1}{2}\mathbf{z}^*\mathbf{K}_0\mathbf{z}\right)}p(spike) \propto \exp\left(-\frac{1}{2}\mathbf{z}^*(\mathbf{K}_{spike}-\mathbf{K}_0)\mathbf{z}\right)$$

Thus the probability of a spike is modulated by a multivariate phase distribution with coupling parameters $\mathbf{K}_\Delta = \mathbf{K}_{spike} - \mathbf{K}_0$. The two coupling matrices $\mathbf{K}_0$ and $\mathbf{K}_{spike}$ can be estimated as described in *SI Methods 4*. $\mathbf{K}_0$ is estimated from the time series of

all phase measurements, $\boldsymbol{\theta}(t)$, and $\mathbf{K}_{spike}$ is estimated from phase measurements at spike times $\{\boldsymbol{\theta}(t)|t = t_{spike}\}$.

The coupling matrix $\mathbf{K}_\Delta$ encodes the neuron-specific preferred pattern of phase coupling, as shown in Fig. 2*H*, and can be thought of as a *phase-coupling receptive field*. The dependency of the coupling-based spike rate $r(\boldsymbol{\theta}; \mathbf{K}_\Delta)$ can then be expressed in terms of the phase-dependent differential energy:

$$\log r(\boldsymbol{\theta}; \mathbf{K}_\Delta) \propto -\mathbf{E}(\boldsymbol{\theta}; \mathbf{K}_\Delta) = -\frac{1}{2}\mathbf{z}^*\mathbf{K}_\Delta\mathbf{z}.$$

We then find a linear regression of $\log r(\boldsymbol{\theta}; \mathbf{K}_\Delta)$ against $-E(\boldsymbol{\theta}; \mathbf{K}_\Delta)$ yielding two parameters, a and b, where $\log r(\boldsymbol{\theta}; \mathbf{K}_\Delta) = -a\mathbf{E}(\boldsymbol{\theta}; \mathbf{K}_\Delta) + b$. This relationship can then be used to predict the neural spike rate given the state of the multidimensional LFP phase.

6. Analysis: Determining Independent Components of the Population Phase Coupling. To investigate the relationships among the phase-coupling receptive fields of individual neurons we apply independent components analysis (ICA) to the ensemble of the logarithm of coupling-based predicted spike rates. We denote the ensemble of the logarithm of coupling-based predicted spike rates as the vector $\mathbf{v}$, where $v_i = \log r_i(\boldsymbol{\theta}; \mathbf{K}_{\Delta,i})$ and i indexes the neuron-specific rate, r_i, and differential coupling matrix, $\mathbf{K}_{\Delta,i}$. Under the ICA model the observations, v_i, are a linear mixture of N_{ICA} sources, s_j, such that

$$v_i = \sum_{j=1}^{N_{ICA}} A_{ij}s_j.$$

Given a set of observations from different time points, we can estimate the mixing matrix $\mathbf{A}$ using standard techniques (9). We can then determine the estimated sources as

$$\mathbf{s} = \mathbf{A}^T\mathbf{v}$$

given an observation vector, $\mathbf{v}$, where the unmixing matrix, $\mathbf{A}^T$, is given by the transpose of the mixing matrix. Because the ICA model produces a linear mixture, each source component can be reexpressed to show that it is selective for a specific phase coupling relationship. By substituting the neuron-specific coupling into the rate we arrive at

$$s_j = \sum_{i=1}^{N_{ICA}} A_{ij}\log r_i\big(\boldsymbol{\theta}; \mathbf{K}_{\Delta,i}\big) = -\frac{1}{2}\mathbf{z}^*\mathbf{K}_{ICA,j}\mathbf{z}$$

$$K_{ICA,\,j} = \sum_{i=1}^{N_{ICA}} A_{ij}\big(a_i\mathbf{K}_{\Delta,i}\big),$$

where we use the regression relation $\log r_i(\boldsymbol{\theta}; \mathbf{K}_{\Delta,i}) = -a_i\mathbf{E}(\boldsymbol{\theta}; \mathbf{K}_{\Delta,i}) + b_i$ as determined in the previous section for each neuron and ignoring the constant offset b_i. Therefore, each ICA source, s_j, is selective for a specific phase coupling pattern, $K_{\text{ICA},j}$, in the LFP. Depending on the statistics of the neural ensemble these sources may represent phase coupling patterns that are relevant only for a single neuron or may capture shared coupling preference among multiple neurons. As we show in Fig. 3*G*, we find that a small number of components are predictive of the majority of neurons, indicating that phase coupling preferences are shared among the neural population.

7. Analyses for Specific Figures. Figs. 2*A* and 4 *E–H* each show the dependence of spiking in a single neuron upon LFP phase for a set of distinct LFP channels recorded simultaneously. Importantly, this analysis considers each LFP channel separately and does not attempt to model effects due to phase coupling between different channels. To generate these figures, first frequency-specific phases were extracted as describe in *SI Methods 3*. One hundred twenty-eight logarithmically spaced center frequencies were used, ranging from 0.3 to 64 Hz. For each center frequency, a constant fractional

bandwidth of 0.325 was used for filtering. Second, for each LFP channel and center frequency the set of phases occurring at the spike times of the neuron of interest was used to estimate the von Mises distribution parameters μ and κ, circular variable analogs to the Gaussian distribution mean and variance. μ indicates the mean angle whereas κ, a measure of dispersion, encodes the concentration of the distribution around μ. This estimation was done using the fitting algorithm described in *SI Methods 4* for which code is available online at ref. 7. Third, the von Mises concentration parameter κ, encoding the concentration of the probability density function prob(θ | spike), and the overall mean spike-count rate, encoding prob(spike), were combined using Bayes' rule to estimate prob (spike | θ). Unlike in *SI Methods 5*, here θ is a univariate phase variable. The percentage of modulation in spike rate was calculated from this PDF, defined as 100 × the difference in maximum and minimum spike rates divided by the mean spike-count rate. Fourth, the percentage of modulation in spike rate was calculated for all center frequencies and LFP channels for all neurons examined in this study. Fig. 2*A* shows the results for one neuron from subject P; Fig. 4 *E–H* shows the results for four simultaneously recorded neurons from subject B.

Fig. 4*I* shows rate modulation vs. frequency traces for all 813 neurons examined in this study after normalization and sorting. For each neuron, first the LFP channel from the microelectrode used to record spike times of that neuron was removed and then the LFP channel showing the maximum modulation was found from the remaining traces. Second, this trace was divided by the maximum modulation value to scale trace values to fall between 0 and 1 to facilitate comparisons across different neurons. Third, the frequency of maximum modulation was identified for each trace and used to reorder traces as a function of modulation frequency.

Fig. 2 *B–G* shows examples of spike-triggered empirical and isolated phase PDFs. To estimate empirical PDFs for particular phase variables (black traces in Fig. 2 *B–D*), von Mises distribution parameters μ and κ were estimated using the set of phases observed on a given LFP channel during spike times. Similarly, von Mises distributions were also used to estimate empirical PDFs for phase differences between two channels (black traces in Fig. 2 *E–G*). To generate isolated PDFs for these variables (red traces in Fig. 2 *B–G*), the matrix $\mathbf{K}_{\text{spike}}$ representing the spike-triggered pattern of phase coupling for a given neuron was estimated as described in *SI Methods 5*, with code available at ref. 7. This estimate takes into account both the direct interaction between pairs of phase variables and indirect interactions through the rest of the network. Therefore, using this estimate we can easily separate out the parameters of the corresponding isolated distribution: They are given by the corresponding parameters κ_{ij} and μ_{ij}. This procedure produces a univariate phase PDF of von Mises form representing either the absolute LFP phase (red traces in Fig. 2 *B–D*) or LFP–LFP phase differences (red traces in Fig. 2 *E–G*).

Fig. 2*H* shows a representation of the preferred pattern of phase coupling for one neuron and was generated from the matrix $\mathbf{K}_\Delta$, which was computed as described in *SI Methods 5*. Nodes represent phase variables and are color coded by area. Links represent coupling between phase variables. The width/contrast of links is proportional to the absolute value of the entries in the matrix $\mathbf{K}_\Delta$. Node size is proportional to the sum of the weights on links entering that node. Plotting of Fig. 2*H* was done using the Python programming language package NetworkX (http://networkx.lanl.gov/).

Fig. 2 *I* and *J* shows the correlation between the predicted coupling-based rate and the measured rate. To generate Fig. 2 *I* and *J*, first a set of training data was used to estimate the coupling matrix $\mathbf{K}_\Delta$; second, LFPs from two different test sets of data were used to generate coupling-based rates for a given neuron, as described in *SI Methods 5*. Third, a binary time series representing the spike train of that neuron was generated. This time series had the same number of sample points as the coupling-based rate (N_{time}) and had a value of 1

at spike times and 0 at other times (no spiking). Fourth, to facilitate an upcoming binning procedure using 200 bins, these time series were truncated to size $N_{\text{tr}} \times 1$, where $N_{\text{tr}} = N_{\text{time}} - \text{mod}(N_{\text{time}}, 200)$; that is, $\text{mod}(N_{\text{tr}}, 200) = 0$. Fifth, the coupling-based rate and spike train were combined to form a single $N_{\text{tr}} \times 2$ matrix C. Sixth, the rows of C were sorted as a function of the values of the coupling-based rate, such that the first column of C is a nondecreasing monotonic function consisting of sorted values of the coupling-based rate (sortrows.m in MATLAB). The second column of C is a binary vector representing reordered spike times. Seventh, C was reshaped into a 3D array of size ($N_{\text{tr}}/200$, 200, 2). Eighth, C was separated into two matrices $C1$ and $C2$, both of size ($N_{\text{tr}}/200$, 200). $C1$ consisted of sorted and reshaped coupling-based rate data and $C2$ consisted of the sorted and reshaped binary data corresponding to the spike train. Ninth, the mean of $C1$ over the first dimension was taken, producing a 200×1 vector of mean predicted rates, where each entry corresponds to the average of 1 of 200 equal-count bins. That is, each bin has an equal number of sample points ($N_{\text{tr}}/200$) and each bin captures one-half percentile of the full range of coupling-based rates. Tenth, a 200×1 vector of measured rates was generated from $C2$ by taking the sum of $C2$ over each column (the number of spikes occurring in each bin), divided by the number of rows (the number of 1-ms sample points within each bin), multiplied by the sampling rate of 1,000 Hz. This procedure produces a value with units of spikes per second. Eleventh, the 200×1 mean predicted rate vector was used as a regression predictor for the 200×1 measured rate vector, with the fraction of explained variance (r^2) and the associated uncorrected P value recorded. Finally, the predicted and measured rates were normalized by subtracting the minimum value and dividing by the maximum value. To summarize, after generating a coupling-based rate, all time samples where the value of the coupling-based rate falls within a narrow bin were identified, and then the number of spikes occurring at these sample points was noted and used to calculate a measured rate that can be compared with the predicted, coupling-base rate.

For Fig. 3, coupling-based rates were generated for 4 neurons as described in *SI Methods 5*. Fig. 3 *B* and *D* shows 2-s examples of coupling-based rates. For Fig. 3*E*, first the correlation coefficients between coupling-based rates were calculated for all 138 simultaneously recorded neurons in one session from subject P, generating a 138×138 correlation matrix C. Second, the interneuron distance for all pairs of neurons occurring within one cortical area was determined. Third, interneuron distance was used as a regression predictor for the correlation coefficients, resulting in a nonsignificant regression. Fourth, pairs of neurons were assigned to one of nine bins on the basis of interneuron distance. Fifth, the mean correlation coefficient for all pairs within one bin was calculated, as well as the SEM (through bootstrap resampling). For Fig. 3*F*, first the tuning direction of each neuron was estimated using cosine fits to the target-specific spike rates for each neuron. Directional tuning was estimated by comparing the mean firing rate as a function of target angle during execution of the movement. The first 2 s of each trial were used. A similar method was also used for shorter time windows (e.g., 200 ms). Essentially identical results were obtained with window sizes of 1 and 1.5 s. The tuning curve was estimated by fitting the firing rate with a sine and a cosine as

$$f = [B_1\,B_2\,B_3] \times \begin{bmatrix} 1 \\ \sin\theta \\ \cos\theta \end{bmatrix},$$

where θ corresponds to reach angle and f corresponds to the firing rate across the different angles. Linear regression was used to estimate the B coefficients. The preferred direction (PD) was calculated using the following: $\text{PD} = \tan^{-1}(B_2/B_3)$, resolved to the correct quadrant. The depth of modulation was measured by calculating the difference between the maximum and the

minimum of the tuning curve (in hertz). B_1 was taken to be the mean firing rate for a session. Second, the absolute difference in tuning direction was determined for each pair of neurons. Third, the difference in direction tuning was used as a regression predictor for the correlation coefficients between coupling-based rates. Fourth, neuron pairs were binned into one of nine bins as a function of tuning difference. Fifth, the mean (and SE) correlation coefficient for all pairs within one bin was calculated.

For Fig. 3G, first the $138 \times N_{\text{time}}$ matrix of coupling-based energies $-E(\theta; \mathbf{K}_\Delta)$ for all simultaneously recorded neurons in one session from subject P was generated as described in *SI Methods 5*. Second, ICA was performed on this matrix, using the runica.m function from the EEGLAB toolbox (10). Third, as described in *SI Methods 6*, the ICA unmixing matrix was applied directly to the preferred phase-coupling network matrix $\mathbf{K}_\Delta$ to generate a set of 138 ICA-component–specific phase-coupling network matrices, each of size 49×49. Fourth, phase data for a new set of test data were generated as described in *SI Methods 3*. Fifth, the ICA-component–specific phase-coupling networks were applied to these phase data to generate an ICA-component–specific, coupling-based energy time series. Sixth, coupling-based rates were generated from these energy series as decribed in *SI Methods 5*. Seventh, each ICA-component–specific coupling-based rate was tested against the spike times of the 138 neurons (see predicted rate/measured rate methods in Fig. 2 *I* and *J*) to determine the percentage of neurons significantly predicted by each component. Eighth, a small set of highly predictive ICA components (red in Fig. 3G) was identified by inspection.

For Fig. 3H, first the $138 \times N_{\text{time}}$ matrix of *I* time series for all simultaneously recorded neurons in one session from subject P was generated as described above. Second, all values for ICA components will low predictive efficacy (black in Fig. 3G) were set to zero. Third, the inverse of the ICA unmixing matrix was used project the

activity of the remaining ICA components upon each of the 138 neurons. That is, each neuron-specific coupling-based energy time series is a linear combination of ICA-component–specific coupling-based energy time series, and the above procedure retains only the ICA components with high predictive efficacy (red in Fig. 3G). Fourth, these energies were used to generate coupling-based rates, as described in *SI Methods 5*. Fifth, the 138×138 matrix of correlation coefficients between these neuron-specific ICA-denoised rates was calculated. Sixth, this correlation matrix was sorted using a clustering algorithm (reorderMAT.m from the Brain Connectivity toolbox: http://sites.google.com/a/brain-connectivity-toolbox.net/bct/visualization).

Fig. 4*A* displays the percentage of neurons exhibiting spike dependence on phase coupling patterns, sorted by functional group. The BMI group consists of 39 M1 neurons directly involved in cursor control (1), whereas the non-BMI group is composed of 62 M1 neurons not involved in cursor control. All neurons were recorded simultaneously. Permutation resampling was used to test for significance.

For Fig. 4*B*, first the $138 \times N_{\text{time}}$ matrix of ICA-component–specific coupling-based rates was generated for each examined BMI data set for subject P. Second, the go-cue onset times for successful BMI trials were identified. Third, epochs starting 2 s before until 4 s after cue onset were extracted for each of the 138 coupling-based components. Fourth, these cue-locked epochs were averaged for each component to generate a time series similar to an event-related potential. Fifth, these traces were smoothed using a Gaussian window (SD of 250 ms). Sixth, the 138 traces were reordered on the basis of the value occurring 100 ms after cue onset. Fig. 4 *C* and *D* shows two of the traces described above (red) as well as peri-stimulus-time histograms (PSTHs). Cue-locked PSTHs were generated in an identical fashion using spike trains rather than ICA components.

1. Ganguly K, Carmena JM (2009) Emergence of a stable cortical map for neuro-prosthetic control. *PLoS Biol* 7:e1000153.
2. Paxinos G, Huang XF, Toga A (2000) *The Rhesus Monkey Brain in Stereotaxic Coordinates* (Academic, San Diego).
3. Kennerley SW, Wallis JD (2009) Reward-dependent modulation of working memory in lateral prefrontal cortex. *J Neurosci* 29:3259–3270.
4. Mann S, Haykin S (1995) The chirplet transform: Physical considerations. *IEEE Trans Signal Process* 43:2745–2761.
5. Cohen L (1995) *Time-Frequency Analysis* (Prentice–Hall, New York).
6. Cadieu CF Koepsell K (2010) Phase coupling estimation from multivariate phase statistics. *Neural Comput*, in press. Available at: http://redwood.berkeley.edu/klab/papers/CadieuKoepsell_PCE_NeuralComp.pdf.
7. Matlab and Python code for phase coupling estimation. Available at http://redwood.berkeley.edu/klab/pce.html.
8. Lachaux JP, Rodriguez E, Martinerie J, Varela FJ (1999) Measuring phase synchrony in brain signals. *Hum Brain Mapp* 8:194–208.
9. Bell AJ, Sejnowski TJ (1995) An information-maximization approach to blind separation and blind deconvolution. *Neural Comput* 7:1129–1159.
10. Delorme A, Makeig S (2004) EEGLAB: An open source toolbox for analysis of single-trial EEG dynamics including independent component analysis. *J Neurosci Methods* 134:9–21.
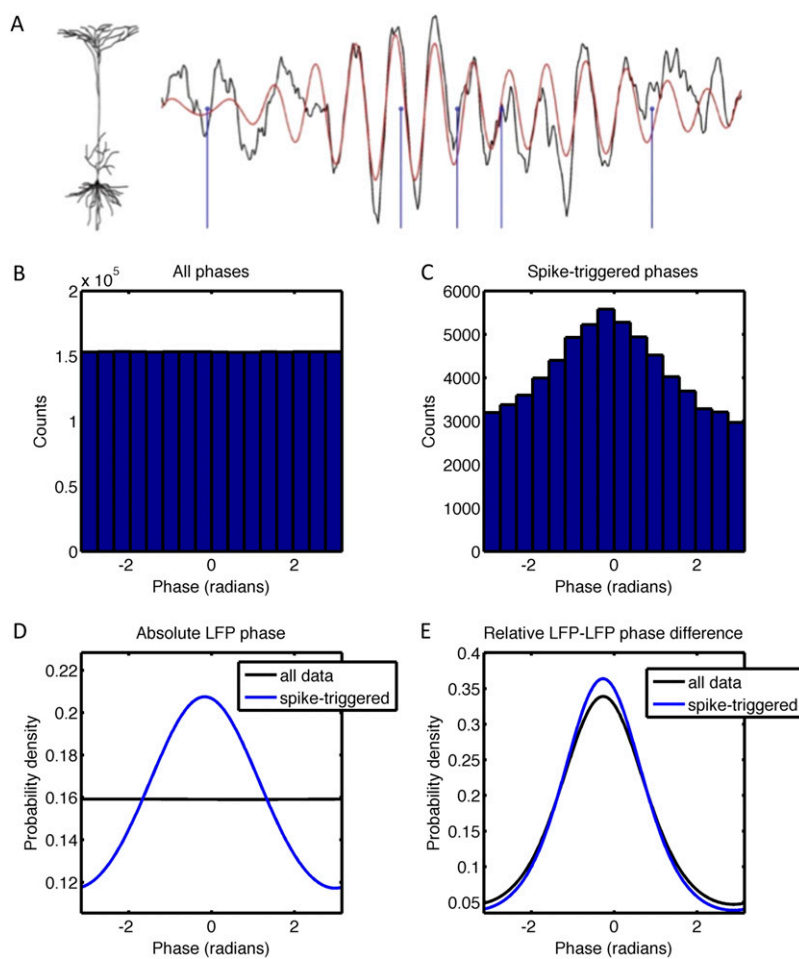
Fig. S1. Example of phase extraction and identification of spike-triggered phases. (*A*) A 1-s example spike train. Spike times are indicated by vertical lines. (*B*) LFP trace from a different microelectrode, filtered with a center frequency of 36 Hz and a fractional bandwidth of 0.325. Spike times are indicated as red dots. (*C*) Amplitude envelope of of filtered LFP trace. (*D*) Phase time series extracted from filtered LFP trace. Phase values range from $-\pi$ to π. Red dots indentify spike times and define the spike-triggered LFP phases.

Fig. S2. (*A*) Example of raw LFP trace (black) and filtered LFP trace (red), with neuronal spike times marked (blue). (*B*) Phases extracted from filtered LFP often exhibit a uniform distribution, as indicated by the histogram. (*C*) In contrast, phases that occur at spike times often concentrate around a preferred phase. (*D*) Probability density functions (PDFs) for phase estimated from all data (black) or at spike times only (blue) often differ, indicating mutual information between spike timing and LFP phase. (*E*) Similarly, PDFs of the phase difference between two LFP channels may differ when all data are considered (black) versus spike times alone (blue).
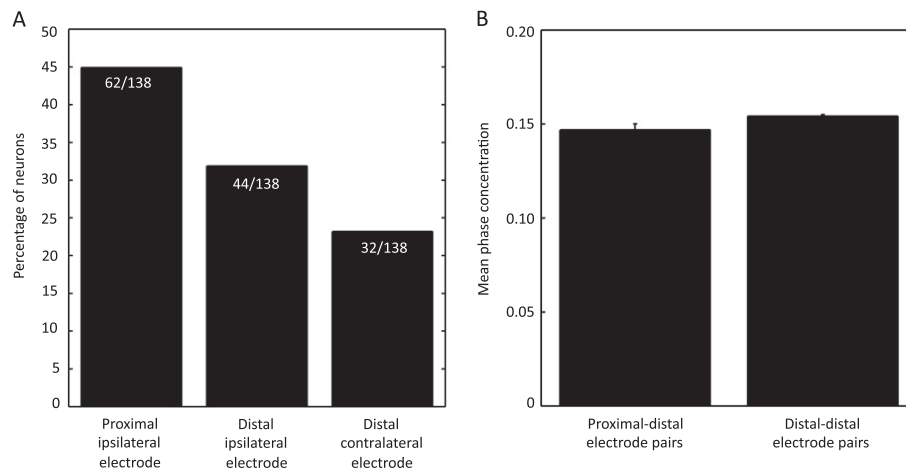
Fig. S3. Spikes depend on proximal LFP phases, distal LFP phases, and LFP–LFP phase coupling between electrode pairs. (*A*) Even after accounting for the proximal LFP phase near the cell body, a majority of neurons (55.1% or 76/138) are more strongly coupled to distal LFP phases than to the proximal LFP phase. Bars show the percentage of neurons where the strongest coupling to (absolute) LFP phase fell into one of three groups. LFP electrodes were classified as proximal to the electrode used to record neuronal spikes if the interelectrode distance was <0.75 mm. A total of 45.0% (66/138) of neurons exhibited the strongest coupling to proximal LFP phase. Distal ipsilateral LFP electrodes were >0.75 mm from the neuron electrode, with a maximum of 9 mm separation in this study. A total of 31.9% (44/138) of neurons were most strongly coupled to a distal ipsilateral LFP phase. Distal contralateral LFP electrodes were in the opposite hemisphere (several centimeters), with 23.2% of neurons locking most strongly to a distal contralateral LFP phase. (*B*) The strength of distal–distal LFP–LFP phase coupling preferred by a neuron is comparable to the strength of proximal–distal LFP–LFP phase coupling preferred by a neuron. For each neuron, the LFP signal from the closest electrode was identified (maximum separation of 0.75 mm), and the mean preferred phase coupling between this proximal LFP signal and all other (distal) LFP signals was computed. Similarly, the mean preferred phase coupling between all pairs of distal electrodes was computed and is shown here to be of comparable magnitude. This result suggests that neurons in one location may nonetheless exhibit sensitivity to the magnitude and angle of phase coupling between LFPs in two distant sites.
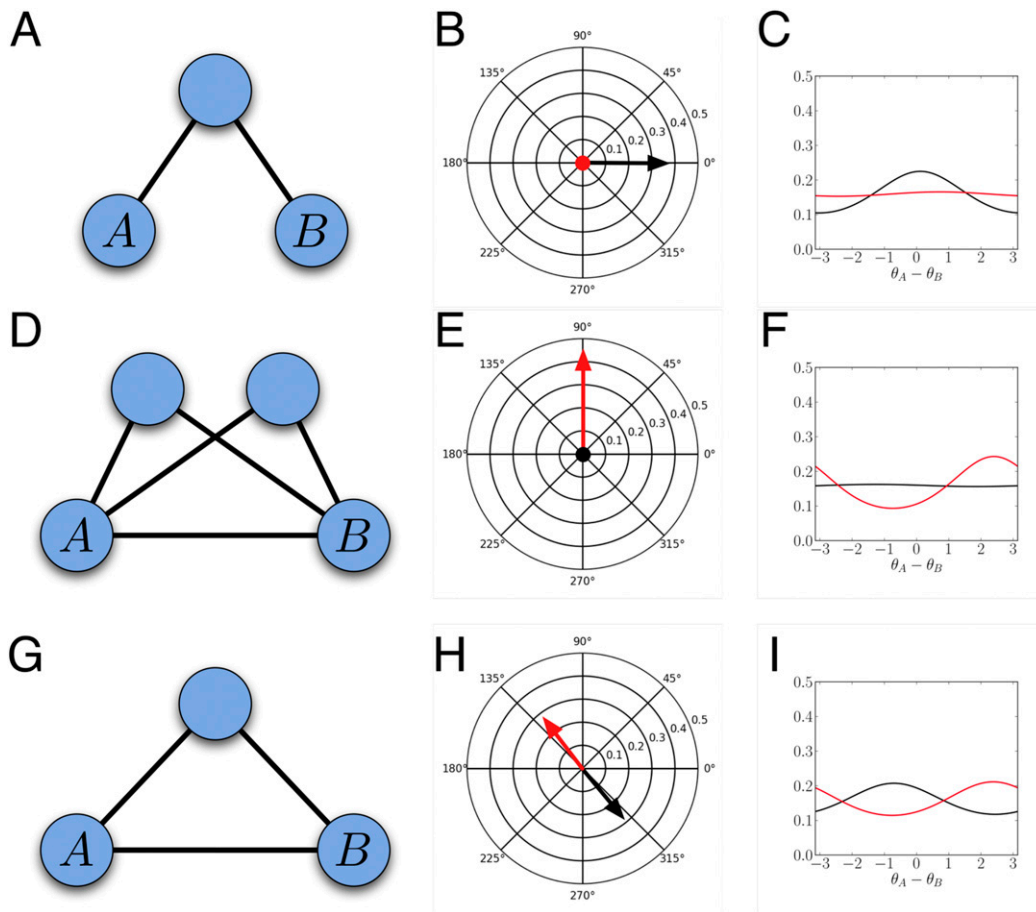
Fig. S4. Phase coupling estimation correctly estimates phase coupling in networks where phase concentrations are misleading. Here we show three example networks (one in each row). The first column (*A*, *D*, and *G*) shows the network coupling used to simulate a system of oscillators. The second column (*B*, *E*, and *H*) indicates the measured phase concentration (black vector) and estimated phase coupling (red vector) between oscillators *A* and *B*. The magnitude and angle of the phase concentration are plotted on the polar plot with angle equal to $\Delta_{A,B}$ and radius equal to $\Upsilon_{A,B}$. The estimated phase coupling, $\kappa_{A,B}$, and angle, $\mu_{A,B}$, are plotted similarly. The third column indicates the isolated distribution $p_{iso}(\theta_A - \theta_B; \kappa_{A,B}, \mu_{A,B})$ (red line) and the empirical distribution $p(\theta_A - \theta_B)$ (black line) for the phase difference $\theta_A - \theta_B$. (*A–C*) *Spurious coupling*: phase concentration measurements (black vector and black line) indicate interaction between *A* and *B* when the true coupling and the estimated coupling (red vector and red line) have 0 magnitude. (*D–F*) *Missing coupling*: phase concentration indicates a lack of coupling between *A* and *B*, but the estimated phase coupling and true phase coupling indicate a strong interaction. (*G–I*) *Incorrect phase offset*: phase concentration indicates that oscillator *A* leads oscillator *B*; however, the true interaction and the estimated phase coupling indicate that oscillator *A* lags behind oscillator *B*.
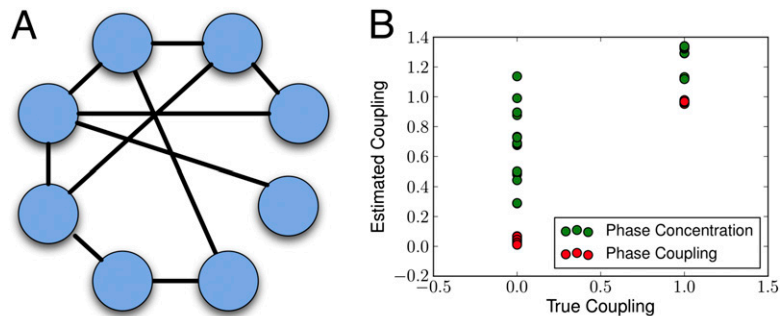

Fig. S5. Phase coupling estimation correctly infers phase coupling in complex networks. (*A*) A network of eight oscillators where solid lines indicate a coupling interaction of $\kappa_{ij} = 1$ and $\mu_{ij} = 0$ and no line indicates that $\kappa_{ij} = 0$ (no coupling). (*B*) The measured phase concentration (green dots) and the estimated phase coupling (red dots) for all pairs of oscillators plotted against the true coupling in the simulated network (*x* axis). Phase coupling estimation correctly recovers the presence of coupling or lack of coupling. Phase concentration includes contributions from the direct interaction between the oscillators and through the network of oscillators and therefore does not reflect the direct interaction.
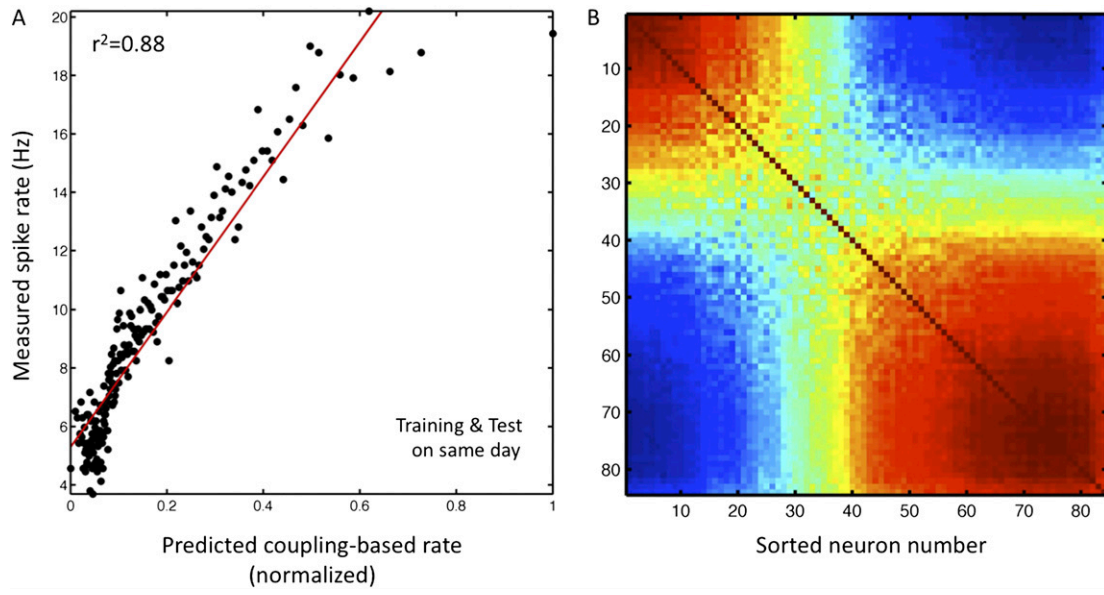
Fig. S6. (*A*) As in Fig. 2 *I* and *J*, for one neuron from subject R. Relationship between predicted coupling-based rate and measured rate is shown. (*B*) As in Fig. 3*H*, for subject R. Correlation matrix between coupling-based rates is shown for the 84 simultaneously recorded neurons.